Latent heating profiles from GOES-16 and its impacts on precipitation forecasts

Yoonjin Lee[1], Christian D. Kummerow[1,2], Milija Zupanski[2]

[1]Department of Atmospheric Science, Colorado State University, Fort Collins, Colorado, 80521, USA
5 [2]Cooperative Institute for Research in the Atmosphere, Fort Collins, Colorado, 80521, USA

Correspondence to: Yoonjin Lee (yoonjin.lee@colostate.edu)

Abstract. Latent heating (LH) is an important quantity in both weather forecasting and climate analysis, being the essential factor affecting intensity or structure of convective systems. Yet, inferring LH rates from our current observing systems is challenging at best. For climate studies, LH has been retrieved from the Precipitation Radar on the Tropical Rainfall Measuring
10 Mission (TRMM) using model simulations in the look-up table (LUT) that relates instantaneous radar data to corresponding heating profiles. These radars, first on TRMM and then Global Precipitation Measurement Mission (GPM), provide a continuous record of LH. However, temporal resolution is too coarse to have significant impacts on forecast models. In operational forecast models such as High-Resolution Rapid Refresh (HRRR), convection is initiated from LH derived from ground based radar. Despite the high spatial and temporal resolution of ground-based radars, their data are only available over well-observed land
15 areas. This study develops a method to derive LH from the Geostationary Operational Environmental Satellite-16 (GOES-16) in near-real time. Even though the visible and infrared channels on the Advanced Baseline Imager (ABI) provide mostly cloud top information, rapid changes in cloud top visible and infrared properties, when formulated as a LUT similar to those used by the TRMM and GPM radars, can equally be used to derive LH profiles for convective regions based on model simulations with a convective classification scheme and channel 14 (11.2μm) brightness temperatures. Convective regions detected by GOES-16
20 are assigned LH profiles from the LUT, and they are compared with LH from the Next Generation Weather Radar (NEXRAD) and one of the Dual-frequency Precipitation Radar (DPR) products, the Goddard Convective-Stratiform Heating (CSH). LH obtained from GOES-16 show similar magnitude with LH derived from the NEXRAD and CSH, and vertical distribution of LH is also very similar with CSH. A three-month analysis of total LH from convective clouds from GOES-16 and NEXRAD shows good correlation between the two products. Finally, LH profiles from GOES-16 and NEXRAD are applied to WRF simulations
25 for convective initiation and their results are compared to investigate their impacts on precipitation forecasts. Results show that LH from GOES-16 have similar impacts as NEXRAD for improving the forecast. While only a proof of concept, this study demonstrates the potential of using LH derived from GOES-16 for convective initialization.

1 Introduction

As the spatial resolution of numerical weather prediction (NWP) models becomes finer, and even operational models are run at
30 convection permitting resolutions of a few kilometers, an effective way to assimilate observation data at this fine resolution has been sought (Gustafsson et al., 2018). Along with the data assimilation, initializing cloud and precipitation in the right location is an important procedure in short-term forecasts (Geer et al., 2017), and modelers seek to use observation data that will create a favorable convection environment at this fine resolution. If the model environment is not favorable for convection, updrafts and clouds will not develop in the right place. Latent heating (LH) can be added in the model data assimilation cycle to help correctly
35 initiate convection in operational regional models where both accuracy and speed are important. Adding LH induces lower level convergence and upper level divergence, thereby initiating convection, and it has become an important procedure that many

operational models use for the initialization of convective events (Weygandt and Benjamin, 2007; Gustafsson et al., 2018). LH is not only important to initiate convection, it also contributes to the intensification of convection.

40   The National Oceanic and Atmospheric Administration (NOAA)'s operational models, the Rapid Refresh (RAP) and High-Resolution Rapid Refresh (HRRR), both use observed latent heating to drive convection, but in different ways (Benjamin et al., 2016). RAP uses digital-filter initialization (Peckham et al., 2016) while HRRR replaces modeled temperature tendency with the observed LH (Benjamin et al., 2016) from the Next Generation Weather Radar (NEXRAD), which is a ground-based radar network over the United States. For this operational purpose, LH data must be available continuously in near-real time.

45   Therefore, ground-based radars which have high spatial and temporal resolutions similar to HRRR's resolution are used to calculate LH from NEXRAD reflectivity. While suitable for the HRRR region over the Contiguous United States (CONUS), the method is not applicable to regions beyond radar coverage such as the Gulf of Mexico and some mountainous areas.

    Satellite data are used to infer climatology of LH over the globe. CloudSat which carries a W-band radar that is sensitive to light

50   precipitation but experiences attenuation with heavy precipitation is used to derive LH for shallow precipitating regions (Huaman and Schumacher, 2018). Nelson et al., 2016 and Nelson and L'Ecuyer, 2018 created an a priori database using model simulations from the Regional Atmospheric Modeling System (RAMS) and used a Bayesian Monte Carlo algorithms to find the most appropriate LH profiles from the database for shallow convective clouds. For deeper convection, satellites that carry instruments with lower frequencies such as Tropical Rainfall Measuring Mission (TRMM) and Global Precipitation Measurement Mission

55   (GPM) satellites are more appropriate to retrieve LH. The Precipitation Radar (PR) on TRMM was the first meteorological radar in space, designed to provide vertical distributions of precipitation over the tropics (Kummerow et al., 1998). Vertical profiles of LH have been retrieved from its three-dimensional hydrometeor observations. There are several retrieval algorithms using PR: Goddard Convective-Stratiform heating (CSH; Tao et al., 1993), Spectral Latent Heating (SLH; Shige et al., 2004), Hydrometeor heating (HH; Yang and Smith, 1999), and Precipitation Radar Heating algorithm (PRH; Satoh and Noda, 2001). Among these

60   algorithms, CSH and SLH are the two most widely used products. Most recent versions of monthly gridded CSH and SLH products have spatial resolution of $0.25°×0.25°$ and $0.5°×0.5°$ respectively with 80 vertical layers and have been used to provide valuable insights on heat budgets and atmospheric dynamics over the tropics (Schumacher et al., 2004; Chan and Nigam, 2009; Zhang et al., 2010; Liu et al., 2015; Huaman and Takahashi, 2016). The CSH and SLH algorithms have improved since their first development, and both algorithms are also applied to Dual-frequency Precipitation Radar (DPR) data on GPM, the successor of

65   TRMM, to continue the climate record of LH and expand the regions of interest to mid-latitude.

    CSH and SLH both rely on a lookup table (LUT) based on cloud resolving model simulations. Inputs that are used to look for LH profiles in these LUT are different, but their common inputs to the LUT are echo top height and surface rainfall rate as well as convective-stratiform flag. Echo top height is important in determining the vertical depth of heating, and surface rainfall rate is a

70   good indicator for the intensity of maximum heating. Even though the methods use different model simulations to create the LUT, and differ in other details, they seem to exhibit similar distributions when they are averaged spatially or temporally (Tao et al., 2016).

    Although these products have been useful for keeping climate records and understanding impacts of LH in long-lasting systems

75   like tropical cyclones, their temporal resolutions are too low to be used for weather forecasting, especially compared to 2-minute observations available from ground-based radars. The current generation of geostationary observing systems (e.g., GOES-16 and

17, Himawari, GEO-KOMPSAT-2) are required to achieve comparable sampling rates to ground-based radars. The visible (VIS) and infrared (IR) sensor on geostationary satellite, unfortunately, cannot provide as much vertical information as active sensors do in the presence of thick clouds. Nonetheless, the rapid refresh provides important information about a cloud's convective

80 nature. Since the RAP model already uses cloud top information from geostationary data in its forecast (Benjamin et al., 2016), and the HRRR model uses the RAP model outputs as initial and lateral boundary conditions, LH profiles derived from cloud top temperature would be consistent with the model cloud field.

This study examines if cloud top information from the Geostationary Operational-Environmental Satellite-16 (GOES-16)

85 Advanced Baseline Imager (ABI), coupled with convective cloud identification can be sufficient to approximate NEXRAD-derived LH. Following the lead of spaceborne radar LH algorithms, a LUT is created using model simulations. Once convective clouds are determined by using 10 consecutive one-minute ABI data, LH profiles for convective clouds are found in the LUT based on cloud top temperature of the convective cloud. Unlike DPR products that are not available continuously, ABI data in mesoscale sector mode are provided at one-minute resolution, and thus LH can be obtained from GOES-16 as frequently as

90 NEXRAD, making it possible to initiate convection during the forecast. LH from GOES-16 can be beneficial over the regions without radar coverage such as ocean or mountainous regions where beam blockage by terrain degrades the quality of radar data.

Detailed descriptions of CSH and SLH products from GPM satellite and how NEXRAD converts reflectivity to LH are provided, followed by the retrieval process using GOES-16 ABI. One case study is provided to compare vertical profiles of LH from

95 GOES-16 with other radar products, and statistical results using three-month of data are provided to evaluate whether total convective heating rates from GOES-16 are comparable to the ones from NEXRAD. Lastly, a Weather Research and Forecasting (WRF) simulation using LH from GOES-16 and NEXRAD is presented to compare impacts of LH from the two datasets in convective initialization.

2 Existing LH retrieval methods

100 ### 2.1 Radiosonde networks

LH is not an easily measurable quantity as it is almost impossible to single out temperature changes by phase changes from the total observed temperature changes. However, heat and moisture budget studies have been conducted using sounding network in a field campaigns, and apparent heat sources (Q_1) and apparent moisture sinks (Q_2) from the budget study can be expressed as a function of LH (Yanai et al., 1973; Johnson 1984; Demott 1996). It is achieved using a diagnostic heat budget method which is

105 first presented by Yanai et al. 1973 (Tao et al., 2006). Over a certain horizontal area, Q_1 can be expressed through the equation below that includes LH (Tao et al., 2006).

$$Q_1 - Q_R = \bar{\pi}\left[-\frac{1}{\bar{\rho}}\left(\frac{\overline{\partial \bar{\rho}w'\theta}}{\partial z}\right) - \overline{\nabla \cdot V'\theta'}\right] + \frac{1}{c_p}\left[L_v(c-e) + L_f(f-m) + L_s(d-s)\right] \tag{1}$$

where prime denotes deviations from horizontal averages, which is denoted by upper bar. Q_R is the radiative heating rate, θ is potential temperature, π is non-dimensional pressure, ρ is air density, c_p is specific heat at constant pressure and R is gas constant

110 for dry air. L_v, L_f, and L_s represent the latent heats of condensation, freezing, and sublimation while c, e, f, m, d, and s represent each microphysical process of condensation, evaporation, freezing, melting, deposition, and sublimation, respectively. The last six terms on the right-hand side that include these microphysical processes are LH from phase changes. Since Q_1 can be obtained

using vertical profiles of temperature, moisture, and wind data observed during the field campaign (Tao et al., 2006), the observed Q_1 is used to indirectly validate GPM LH products that are retrieved together with Q_1.

2.2 CSH and SLH from GPM DPR

LH is fundamentally a temperature change resulting from the phase change of water in the atmosphere. Given the difficulties associated with measuring temperature change where condensation is occurring and further attributing those temperature changes to phase changes is not possible on a regular basis. Instead, many methods rely on the detection of hydrometeors, generally from microwave sensors, and then infer the LH from the hydrometeor content. Precipitation observed from microwave sensors and latent heating are closely related, but since hydrometeors are created through condensation, LH derived from a microwave sensor is actually LH that is released at an earlier location before the observation time. However, LH products from ground-based radars, or from a microwave sensor on satellites such as DPR on GPM, can be routinely generated over broad scales, the advantages of which outweigh any time and space mismatch.

DPR has two operational LH algorithms: CSH and SLH. In the GPM products, LH is provided along with additional variables: Q_1-Q_R and Q_2 in SLH and Q_1-Q_R-LH, Q_R, and Q_2 in CSH as well as the rain type (Tao et al., 2019). These algorithms were first developed for TRMM data, but have been adapted to GPM data. Both algorithms use cloud resolving model simulations to create a LUT relating hydrometeor profiles to modeled heating rates. Although there is no direct measurement for LH to validate the results, retrieved Q_1 and Q_2 are compared instead with sounding data from various field campaigns through the method mentioned in Section 2.1. The evolution of these products is well summarized in (Levizzani et al., 2020), but each algorithm is briefly explained here.

The CSH algorithm was first introduced by Tao et al. 1993. The initial algorithm by Tao et al.1993 used surface rainfall rate and amount of stratiform rain as inputs to the LUT, but the LUT has been improved by increasing the number of LH profiles, using finer resolution in simulations, and adding new inputs such as echo-top heights and low-level vertical reflectivity gradients (Tao et al., 2019). For high-latitude regions observed by the GPM satellite, new LUTs have been created with simulations from the NASA Unified-Weather Research and Forecasting model which is known to be suitable for high latitude weather systems (Levizzani et al., 2020). Inputs to this new LUT are surface rainfall rate, maximum reflectivity height, freezing level height, echo top height, decreasing flag (whether or not reflectivity values drop by more than 10dBZ toward the surface), and maximum reflectivity intensity (Tao et al., 2019).

The SLH algorithm is based on Shige et al. 2004 and Shige et al. 2007. For tropical regions, the LUT is created for three different rain types; convective, shallow stratiform, and anvil (or deep stratiform) clouds. Inputs to the LUT are precipitation top height (PTH), precipitation rate at the surface (P_s), precipitation rate at the level that separates upper-level heating and lower-level heating (P_f) and precipitation at the melting level (P_m). Once non-convective rain is separated into either shallow stratiform or anvil, a vertical profile for anvil cloud is chosen based on P_m, and magnitudes of upper level heating and lower level cooling are normalized by P_m and (P_m - P_s), respectively. For convective and shallow stratiform clouds, a vertical profile corresponding to the PTH is chosen, and then upper-level heating and lower-level heating are normalized by P_f and P_s, respectively. For DPR, a new LUT is created for mid and higher latitude to account for expanded latitudinal coverage by GPM. For higher latitude regions, six precipitation types (convective, shallow stratiform, three types of deep stratiform, and other) are used instead of

three, and therefore six respective LUTs exist. Inputs to these LUTs are precipitation type, PTH, precipitation bottom height, maximum precipitation, and P_s.

Figure 1 shows monthly gridded products from these two algorithms over CONUS for July of 2020 at three different heights as
155   well as their vertically integrated heating rates. Overall horizontal patterns in the two products look similar, but there is a difference in the vertical. At 2km or 5km, CSH tends to show higher heating rates than SLH, while at 10km, SLH shows higher heating rates than CSH. In addition, SLH tends to have larger cooling rates throughout the layers. If integrated over the whole vertical layers, CSH tends to show higher heating rates in general. These discrepancies can be attributed to different configuration setup such as microphysical scheme used to run simulations for the LUT. The results demonstrate that the vertical
160   profiles of LH are highly dependent on the simulations that comprise the LUT as well as different inputs to the LUTs.

165

170

175

180

185

190
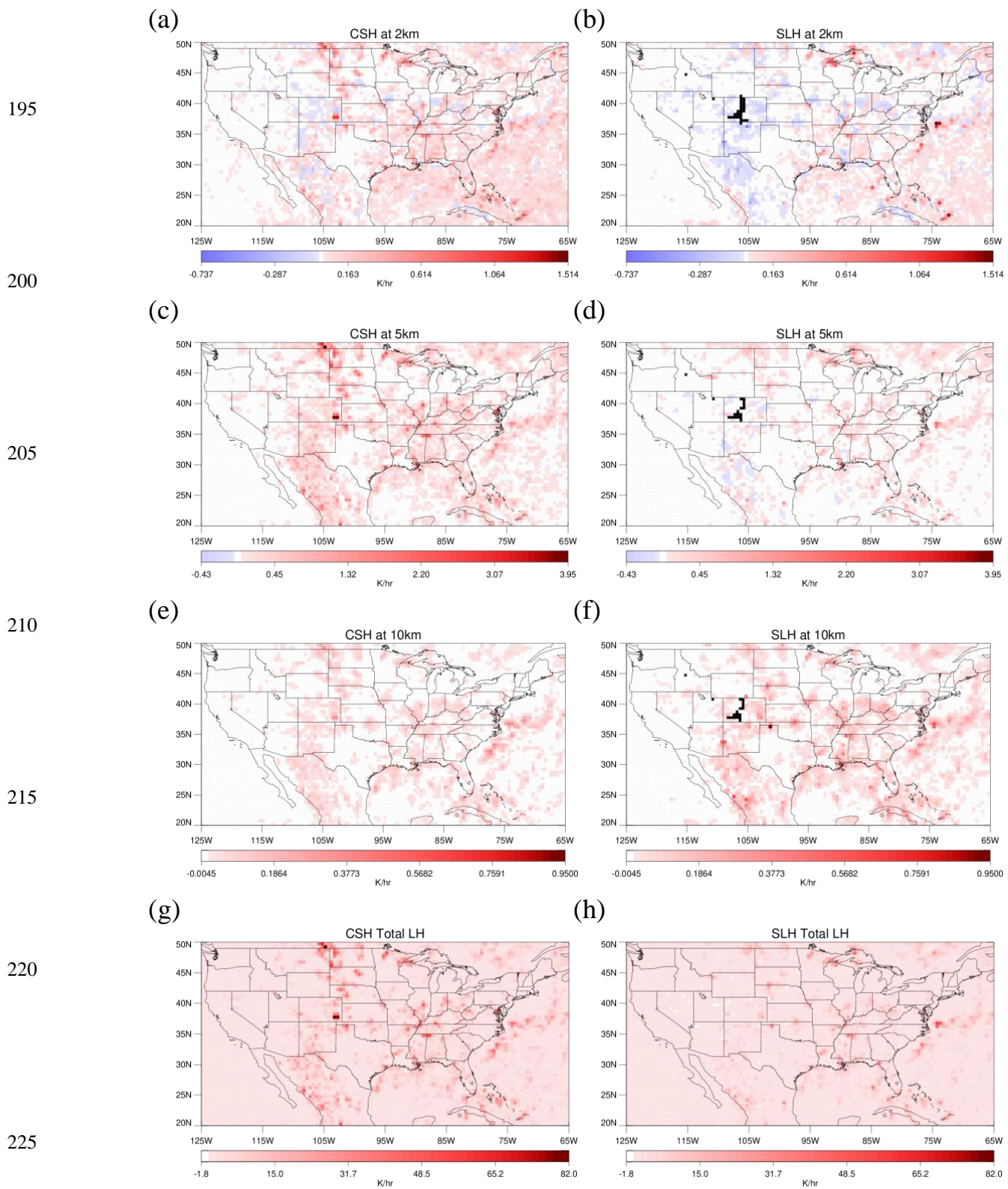
Figure 1: Monthly gridded LH from CSH at (a) 2km, (c) 5km, (e) 10km, and (g) vertically integrated LH from CSH and LH from SLH at (b) 2km, (d) 5km, (f) 10km, and (h) vertically integrated LH from SLH.

Orbital data for these products have finer spatial resolution of 5km, and although results may be interpreted as "instantaneous" LH, the temporal resolution is too coarse to have much impact on regional forecast models that are initialized hourly if not more frequently. These scales are consistent with ground-based radar data which is why LH derived from ground-based radar is used almost universally.

2.3 LH from NEXRAD

In the operational HRRR model, LH profiles retrieved using radar reflectivity replace modeled LH profiles, which helps initiate convection in the right places. LH profiles in this case are obtained through a simple empirical formula that converts radar reflectivity to LH. In Eq. (2), reflectivity is converted to potential temperature tendency using a model pressure field. This equation is only applied when radar reflectivity exceeds 28dBZ. The threshold of 28dBZ was chosen based on the effectiveness of adding heating from reflectivity in HRRR (Bytheway et al., 2017).

$$T_{ten} = \frac{1000^{R_d/c_{pd}}}{p} \frac{(L_v+L_f)Q_s}{n \cdot c_{pd}} \quad \text{where } Q_s = 1.5 \times \frac{10^{z/17.8}}{264083} \qquad (2)$$

  z: grid radar/lightning-proxy reflectivity

  T_{ten}: temperature tendency

  p: background pressure (hPa)

  R_d: specific gas constant for dry air

  c_{pd}: specific heat of dry air at constant pressure

  L_v: latent heat of vaporization at 0°C

  L_f: latent heat of fusion at 0°C

  n: number of forward integration steps of digital filter initialization

T_{ten} in Eq. (2) is produced in K/s to meet the needs during the short-term forecast. Although heating rate is not a general output in the forecast model, it is calculated at every time step by dividing temperature change from the microphysical scheme by the time step, which is usually on the order of few tens of seconds. Therefore, this empirical formula is developed to produce LH consistent with the model framework so that LH added does not produce computational instability when ingested.

3 LH profiles from GOES-16

The current operational geostationary satellite, GOES-16, carries the ABI, an instrument with 16 VIS and IR channels. Mesoscale sectors, which are manually moved around to observe interesting weather events, provide data in one-minute intervals. Such high temporal resolution data have helped observe cloud developments in more detail. Using this high temporal resolution ABI data, convective clouds are detected, and LH profiles for the detected clouds are assigned from a LUT. The LUT is created running the Weather Research and Forecasting (WRF) model simulations. While the CSH and SLH algorithms look for LH profiles in a model-based LUT according to precipitation type and precipitation top height, the LUT for GOES-16 ABI is created for convective clouds that appear bright and bubbling from ABI according to brightness temperature (T_b) at channel 14 (11.2μm), which is a good indicator of cloud top temperature. LH is not assigned for stratiform clouds from GOES-16 as LH from stratiform clouds are not usually used to initiate convection in the forecast model. Once convective clouds are detected using temporal changes in reflectance and T_b, LH profile corresponding to the T_b of the detected cloud is assigned from the LUT.

3.1 Definition of convection in model simulations and GOES-16 ABI

In order to make a LUT for LH profiles of convective clouds, convective grid points need to be defined in the model simulation.

Convection can be defined in several different ways depending on available variables, but the most direct and accurate way of

270   defining it is to use vertical velocity (Zipser and Lutz, 1994; LeMone and Zipser, 1980; Xu and Randall, 2001; Houze 1997; Steiner et al., 1995; Del genio et al., 2012; Wu et al., 2009). Steiner et al., 1995 and Houze 1997 suggested that convective regions tend to have vertical velocity greater than 1 ms^{-1}, and many previous studies that used vertical velocity to define convection used a threshold of 1 ms^{-1} (LeMone and Zipser, 1980; Xu and Randall, 2001; Wu et al., 2009). Similarly, this study uses a vertical velocity threshold to define the convective core as it is one of prognostic variables in the model simulations.

275   However, in this study, a vertical velocity threshold is defined at a layer that has maximum hydrometeor contents. This is intended to exclude potentially high values of negative vertical velocity that can occur at high levels in the cloud if evaporative cooling is present.

To establish the vertical velocity threshold in this study, several values are tested to produce corresponding convective fractions.

280   Those are compared to the convective fractions from the GOES-16 convection detection algorithm (described in Lee et al. 2021), and the vertical velocity threshold whose convective fractions compared best to GOES-16 is chosen. The GOES-16 convection detection algorithm uses mesoscale sector data with one-minute intervals to detect convective regions from ABI imagery. Two separate detection methods are proposed: one for vertically growing clouds in early stages, and one for mature convective clouds that move rather horizontally once they reach the tropopause and often have overshooting tops. A detailed description of the

285   methods can be found in Lee et al. 2021, but it is briefly explained here. The method for vertically growing clouds measures T_b decrease over 10 minutes for two water vapor channels, and if the decrease is greater than the designated threshold (-0.5K/min for channel 8 and -1.0K/min for channel 10), it assigns the pixel as convective. For mature convective clouds, the method looks for grid points that have continuously high reflectance (reflectance greater than 0.8), low T_b (T_b less than 250K), and lumpy cloud top (horizontal gradient values between 0.4 and 0.9) over 10 minutes. Lumpiness of the cloud top is calculated using the

290   Sobel operator, which is commonly used for edge detection. These thresholds are chosen based on one-month analysis against "PrecipFlag" from the Multi-Radar/Multi-Sensor System (MRMS), which classifies precipitation types combining data from ground-based radar and rain gauge observations. Combining the two methods yielded false alarm rates of 14.4% and a probability of detection of 45.3% against the ground-based radar product, but 96.4% of the false alarm cases were at least raining. Combining the two methods provides results comparable to radar product, and these methods are rather simple and fast.

295   These methods detect any type of convective region, and therefore, the analysis is conducted without distinguishing different types of convective clouds.

Table 1 shows convective fractions using the GOES-16 convection detecting algorithm and using different vertical velocity thresholds in the model outputs. Using higher thresholds can eliminate non-convective grid points, but at the same time, it will

300   only include the strongest parts of convective regions. Using 1.5m/s shows a fractional area closest to the observed fraction, and therefore, 1.5m/s is used to define convection in the model output. This number is similar to values used in some previous modeling studies (1m/s in LeMone and Zipser 1980, Xu and Randall 2001, and Wu et al., 2009) and a satellite-based study (2-4m/s in Luo et al., 2014).

305

Table 1. Fraction of convective area in observation and using different vertical velocity thresholds in the model output.

Observation	1m/s	1.5m/s	2m/s	3m/s	4m/s
1.34%	1.86%	1.19%	0.86%	0.52%	0.34%

3.2 Model simulations used to create a lookup table

310 Eleven convective cases are simulated using WRF to obtain enough samples to populate each cloud top temperature bin. The convective cases are chosen over CONUS within the NEXRAD network during May to August in 2017 or 2018. All simulations use the same configuration, shown in Table 2, and HRRR analysis data are used for initial and boundary conditions. All the convective cases are run from the start of convective activity in the scene, for at least several hours depending on the longevity of convective activities for each case, and model outputs are collected every 10 minutes so that the LUT includes LH profiles at all

315 stages and types of convection. However, the LUT is not divided into different types of convection, as it is hard to distinguish convective types from observation. One thing to note is that the magnitude of LH can vary depending on the model configuration such as spatial resolution, time step, and microphysical scheme. This study uses the same model configuration as the HRRR model for all simulations, which avoids discrepancy in magnitude between the modeled LH and the derived LH that will be inserted into the forecast models. T_bs at 11.2μm are calculated using the Community Radiative Transfer Model (CRTM). In each

320 scene, convective grid points are defined by the threshold established in the previous section (1.5m/s), and LH profiles from the convective grid points with the same T_b from channel 14 are averaged to produce mean profiles for each T_b bin of the LUT. LH profiles gathered in the LUT are provided in K/s as for NEXRAD.

Table 2. Table for WRF simulation setup.

Version	WRFv3.9
Spatial resolution	3km
Number of vertical layers	50
Time step	10 seconds
Microphysical scheme	Aerosol-aware Thompson scheme (The original scheme is modified to produce vertical profiles of LH as outputs)
Planetary boundary layer	Mellor-Yamada Nakanishi Niino (MYNN) Level 2.5 and Level 3 schemes
Land surface model	Rapid update cycle (RUC) land surface model
Long wave and short wave radiation physics	Rapid radiative transfer model for general circulation models (RRTMG) schemes

325

3.3 Mean LH profiles according to cloud top temperature

LH profiles of convective clouds from 11 WRF simulations are collected according to 16 bins of the cloud top temperature at 11.2μm. The sixteen bins range from below 200K to above 270K with a bin size of 5K. Figure 2 shows mean vertical profiles of LH in each bin. All profiles exhibit slightly negative LH near the ground due to evaporation, but positive LH is shown at most

330 layers. It is also nicely shown in the figure that as the T_b decreases, the profile stretches up in the vertical. Interestingly though,

the maximum heating rate is not perfectly proportional to T_b. Considering the maximum LH that is allowed in HRRR model, which is 0.01K/s, these values seem quite reasonable. Table 3 shows mean surface precipitation rate for each bin. Precipitation rate is inversely proportional to T_b in Table 3. This is expected as deeper and higher clouds tend to precipitate more. This provides more evidence that mean LH profiles for each bin can reasonably be obtained from GOES-16.

335
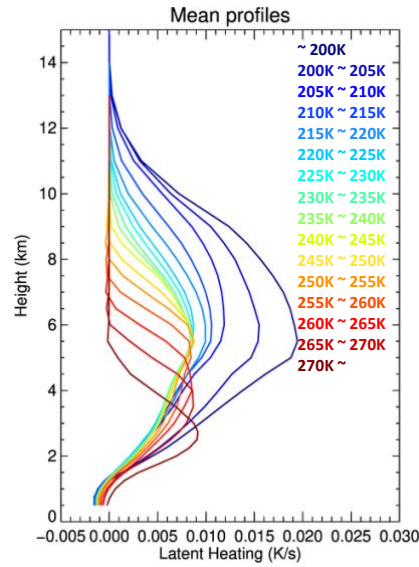
Figure 2: Mean vertical profiles for each cloud top temperature bin.

350   **Table 3.** Table of mean precipitation rate for each cloud top temperature bin.

	Mean precipitation rate (mm/hour)
~200K	48.3
200K ~ 205K	42.9
205K ~ 210K	42.1
210K ~ 215K	37.9
215K ~ 220K	33.6
220K ~ 225K	27.7
225K ~ 230K	21.8
230K ~ 235K	18.8
235K ~ 240K	16.8
240K ~ 245K	16.4
245K ~ 250K	14.0
250K ~ 255K	13.2
255K ~ 260K	11.0
260K ~ 265K	9.2
265K ~ 270K	6.9
270K ~	4.7

The LUT in Fig. 2 is used throughout the later sections, but it can be further divided with additional inputs. Decrease in brightness temperature is one of the options, but it is not considered in this study for several reasons. Since clouds move over time, cloud advection adds uncertainty to the change in brightness temperature if calculated per pixel. In order to measure robust
355 brightness temperature decrease, the decrease can be calculated per cloud, not per pixel; but in such a case, LH profiles will have to be assigned for each cloud, and the assigned profile will be inconsistent with the observed cloud top temperature for each pixel. Therefore, using brightness temperature decrease as additional inputs to the LUT is not included in this study, and it remains as future study. Instead, each cloud top temperature bin can be further divided according to composite radar reflectivity, and the additional LUT is presented in Appendix A. Composite reflectivity, if available, can be used to adjust the maximum
360 intensity of LH profiles as the SLH algorithm adjusts the amplitude by multiplying P_s and P_f. Although it is challenging to get the whole vertical profile of radar reflectivity from GOES-16 data, there are algorithms developed to estimate composite reflectivity from GOES-16, such as GOES Radar Estimation via Machine Learning to Inform NWP (GREMLIN; Hilburn et al. 2021). Therefore, this additional LUT can be used along with such an estimator to assign LH profiles in more detail, but it is not further used in this study.

365 **4 Comparisons of LH profiles between GPR DPR, NEXRAD, and GOES-16 ABI**

4.1 A case study on 18 June 2019

LH from three different instruments, GOES-16 ABI, NEXRAD, and GPM DPR are examined for comparison. Methods using GOES-16 and DPR products are similar in the sense that they use cloud top height or PTH to look for mean profiles in the LUT created with model simulations, although DPR has additional parameters such as surface rain rate which is used to vary the
370 magnitude of the heating rate. In contrast, NEXRAD uses an empirical formula to convert radar reflectivity to LH regardless of PTH. They are all instantaneous heating, but provided in different units. LH from GOES-16 and NEXRAD are in K/s to easily match with modeled heating rate, while DPR products are in K/hour. Therefore, LH in K/hour from DPR products are converted to K/s for comparison.

375 A scene on 18 June 2019 is shown in Fig. 3 to compare how each product determines precipitation type (convective or stratiform) which is one of the major factors in estimating LH profiles. The regions with reflectivity greater than 28dBZ in Fig. 3a are regions where LH is estimated from NEXRAD reflectivity to be used in HRRR, but not necessarily convective regions. Pink regions on top of the visible image at channel 2 (0.65μm) in Fig. 3b are convective regions detected by GOES-16, and represent the smallest regions compared to others. The number of convective grid points from each product after interpolating
380 into the 3km resolution WRF grid is presented in Table 4 for a quantitative comparison. Even though areal coverage differs by the methods, locations of convective core matches well between the products.
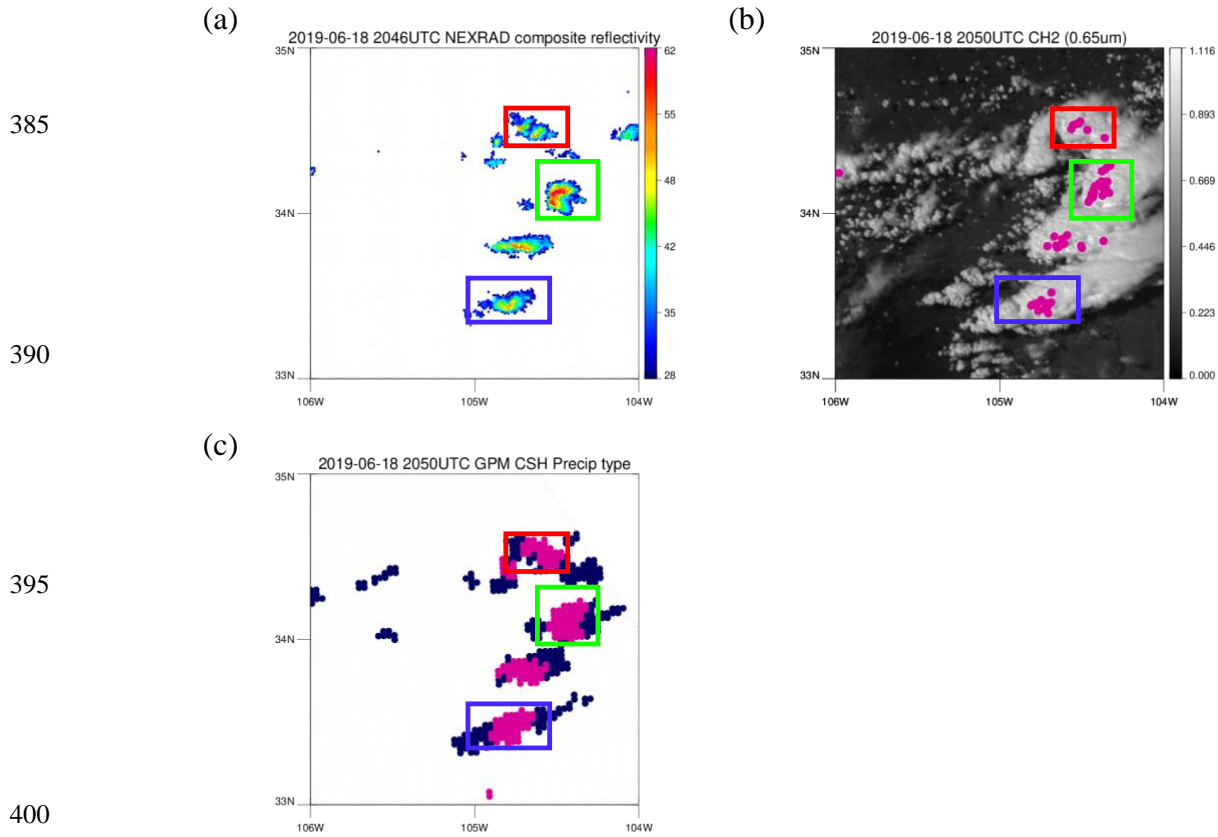
Figure 3: A scene on 18 June 2019. (a) NEXRAD composite reflectivity. Only the regions with reflectivity greater than 28dBZ are shown in colors. Color bar is in dBZ. (b) Convective regions detected by GOES-16 are colored in pink on top of GOES-16 visible imagery of channel 2 (0.65μm) reflectance. (c) Precipitation type defined by CSH. Convective regions are colored in pink while stratiform regions are colored in navy.

Table 4. Total number of grid points from NEXRAD, GOES-16, and CSH in the red, green, and blue box regions after interpolating into the same 3km WRF grid.

	Red	Green	Blue
NEXRAD	30	41	35
GOES-16	15	36	23
CSH	34	50	43

Clouds in the colored boxes in Fig. 3 are all convective clouds, but in different evolutional stages. Clouds in red, green, and blue boxes respectively have high, low, and mid-level cloud top temperature. Since the three products have different spatial resolutions, LH profiles from NEXRAD, GOES-16, and CSH for these clouds are interpolated into the same WRF grid with 3km resolution for a direct comparison in Figs. 4, 5, and 6. CSH provides LH for both convective and stratiform regions, and thus different colors of lines in Figs. 4c, 5c, and 6c represent different cloud type. Lines with light blue color are LH profiles of convective grid points, while the blue line is the mean of these profiles. Similarly, LH profiles of each stratiform gird point are in light green, while the mean of these profiles is in dark green. The mean of all LH profile is colored in red. Convective LH profiles from CSH shows heating throughout the vertical layers as expected, except near the surface due to evaporation at lower levels. LH profiles in stratiform regions show cooling at low levels below a melting level and heating above. LH profiles from GOES-16 (GOES LH) corresponding to the three convective clouds are shown in Figs. 4b, 5b, and 6b. When GOES LH and CSH are compared, the mean profile of convective LH from CSH in blue (Figs. 4c, 5c, and 6c) is similar to GOES LH in blue (Figs. 4b, 5b, and 6b) both in terms of the magnitude and the vertical shape.

On the other hand, LH from NEXRAD (NEXRAD LH) shows a different vertical profile than GOES LH or CSH, which both use the LUT consisting of model simulations. GOES LH or CSH peak around the middle of the atmosphere while NEXRAD LH in the convective core (Figs. 4a, 5a, and 6a) tends to peak at low levels where radar reflectivity is high. At low levels where model simulations have cooling, NEXRAD LH does not show cooling due to Eq. (2) which is designed to only produce positive values. This heating at lower levels induces convergence in the lower atmosphere and divergence in the upper atmosphere, and thus, convection can be effectively initiated from the added heating.

Although their vertical shape is different, the magnitude of the NEXRAD LH is similar to the other products. Overall values of mean LH profile from NEXRAD in blue are slightly smaller than mean profile of GOES LH or mean convective LH profile from CSH (blue line), but are closer to the total mean profile of CSH (red line), which indicates that the 28dBZ threshold might include some stratiform regions as well. A smaller mean of NEXRAD LH is mainly attributed to anvil regions where reflectivity greater than 28dBZ only exist at few vertical layers and reflectivity is equal to 0dBZ elsewhere.

465

470

475
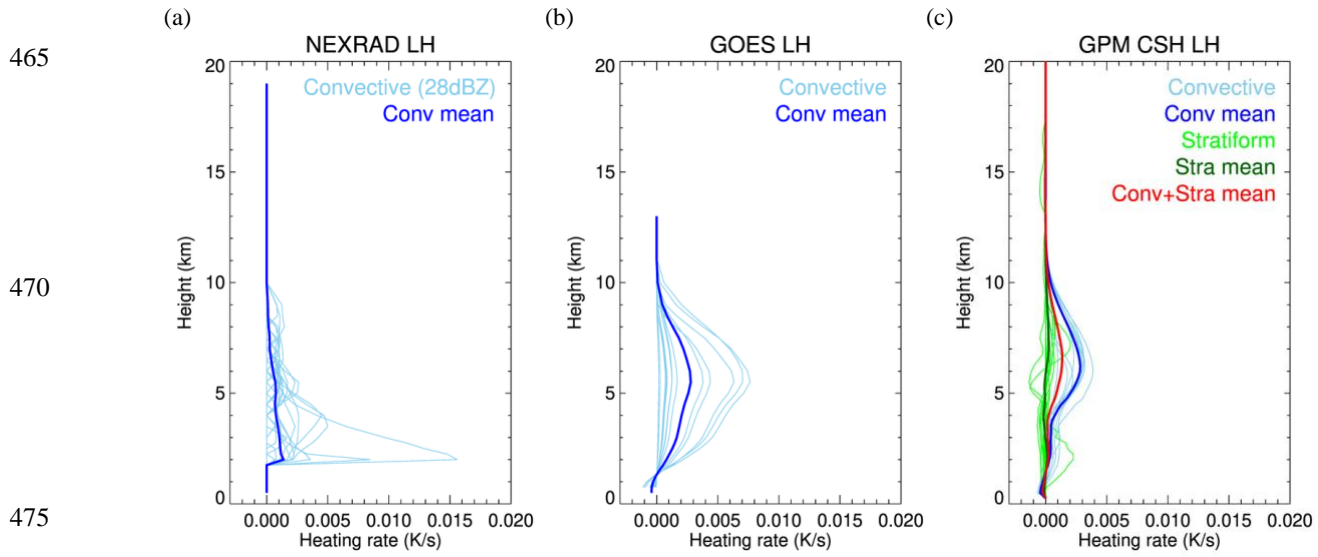
480 **Figure 4: LH profiles from (a) NEXRAD, (b) GOES-16, and (c) CSH for the red box region. Light blue lines are each LH profile for individual convective grid points and the darker blue line is a mean profile of the light blue lines. In (c), the LH profile for each stratiform grid point is coloered in light green and its mean profile is colored in dark green. The mean of all (convective and stratiform) LH profiles for CSH is colored in red.**

485

490

495
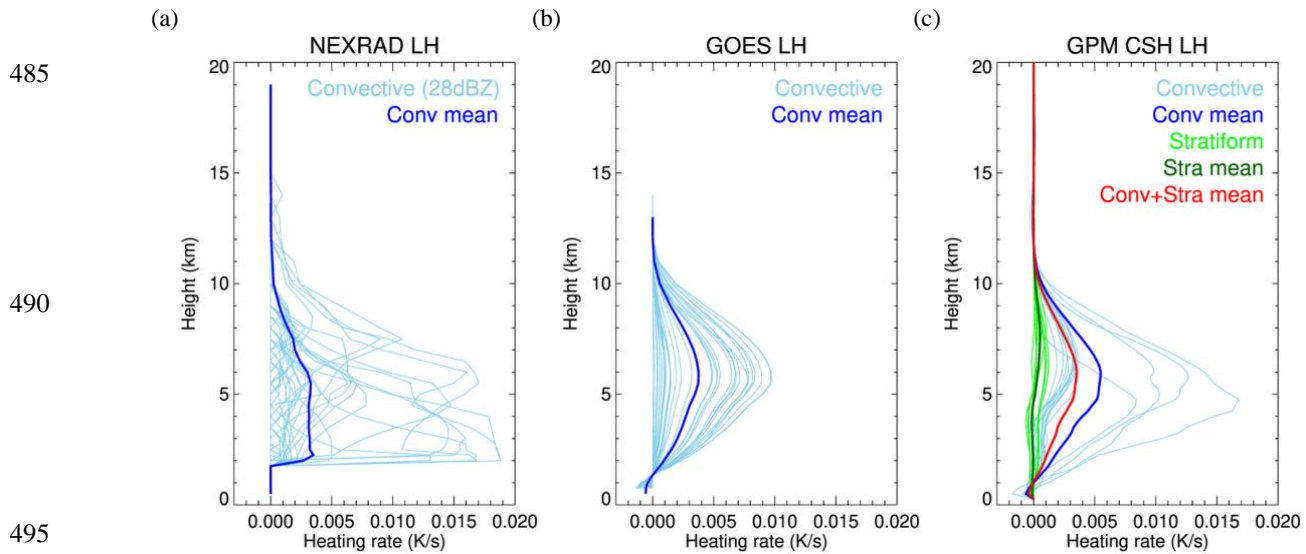
Figure 5: Same as Fig. 4, but for the green box region.

500

505

510

515
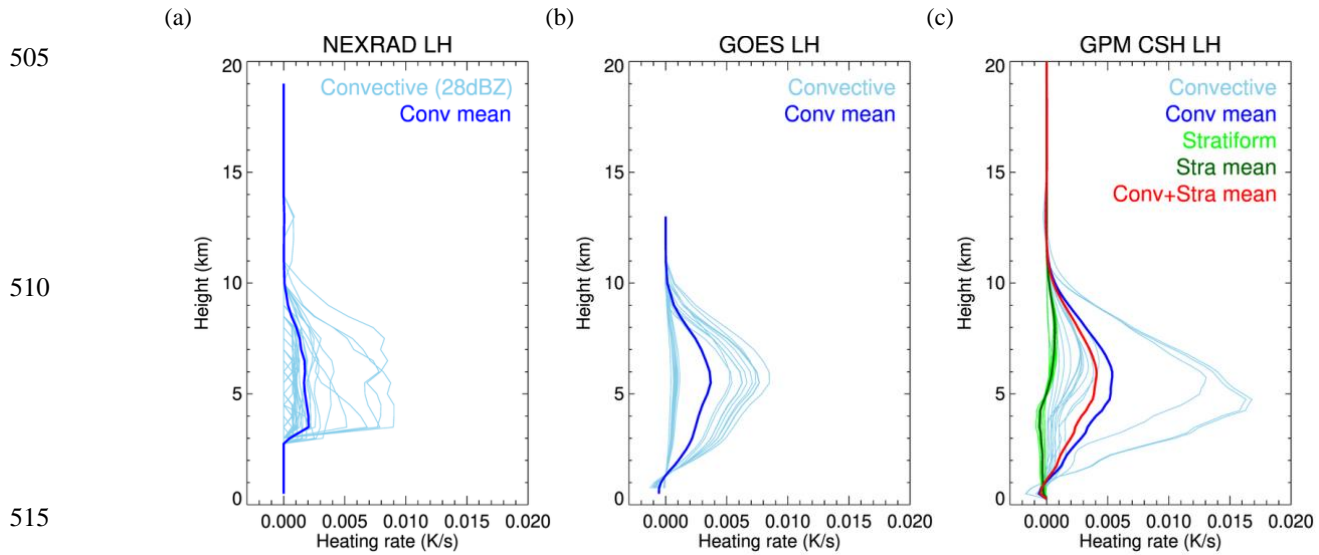
Figure 6: Same as Fig. 4, but for the blue box region.

520

Even though the mean NEXRAD LH is smaller, the total LH for the region can be similar when it is added up over the region due to broader area determined by the threshold of 28dBZ in Fig. 3a than GOES-16 detection in Fig. 3b. Therefore, the total LH of each cloud is again compared between the three products (Table 5). "Total LH" is defined here as vertically and horizontally integrated LH over each convective cloud. The reason why the total LH is used for a comparison is because NEXRAD LH has

525 such a different vertical structure from GOES LH or CSH LH and such different convective areas, that it is difficult to makes direct comparison between vertical levels. In addition, comparing combined values will be meaningful as those are the values that will be used to initiate each convective cloud. Table 5 shows that the total LH from CSH tends to be higher than the other two products, while the total LH is shown to be similar between NEXRAD and GOES-16, although GOES LH is slightly larger. Despite the smaller mean of NEXRAD LH that was shown in Figs. 4, 5, and 6, it shows a good agreement with GOES-in total

530 heating.

Table 5. Total LH (K/s) from NEXRAD, GOES-16, and CSH in the red, green, and blue box regions.

535

	Red	Green	Blue
NEXRAD	0.31	1.41	0.68
GOES-16	0.44	1.52	0.89
CSH	0.84	3.18	2.70

4.2 Three-month analysis against NEXRAD LH

540   A case study from section 4.1 is presented to show how the vertical structure of GOES LH compares to other radar products. In this section, three months of data from May, June, and July of 2020 are used to compare total LH for convective clouds between GOES-16 and NEXRAD. Total LH used in this section is again vertically and horizontally integrated LH over each convective cloud. Both GOES-16 brightness temperature and NEXRAD reflectivity are resampled to the 3km HRRR grid for a direct comparison, and are compared under several conditions that the HRRR model uses to avoid disruption in existing model physics

545   when inserting LH into the model. During the convective initiation step in the HRRR model, LH is calculated form NEXRAD radar reflectivity following Eq. (2) if the layer: is cloudy, is under the GOES cloud top (using Level 2 Cloud Top Pressure data), is above the planetary boundary layer, and has a temperature less than 277.15K. Additionally, LH is calculated for temperatures greater than 277.15K only if the corresponding reflectivity exceeds 28dBZ.

550   GOES LH is calculated with the same criteria described above, except for the additional 28dBZ categorization. Adjacent convective grid points by the detection algorithm are clustered to define a convective cloud. In order to minimize errors coming from different definitions of convection in GOES and NEXRAD, total LH is compared only in clouds where both NEXRAD and GOES detect convection. Since the area defined as convective cloud tends to be wider in NEXRAD than in GOES-16, and one convective cloud from NEXRAD tends to include multiple convective cloud systems defined by GOES, the comparison is done

555   by combining all convective clouds by GOES-16 that overlap with each convective cloud by NEXRAD. Regions with low radar quality, as indicated by the radar quality flag, are excluded in the analysis.

Among 4045 convective clouds collected from the three-month data, only 2660 convective clouds are within reasonable range of each other in both GOES-16 and NEXRAD. We define "reasonable range" here as: the number of convective grid points from

560   GOES-16 does not exceed five times that of NEXRAD and vice versa. Those 2660 clouds are selected, and the total LH from both GOES-16 and NEXRAD for these clouds is fitted into a linear regression model. Figure 7 shows a scatter plot of NEXRAD LH and GOES LH for each convective cloud in log-log axes. A decent correlation coefficient of 0.83 is obtained between NEXRAD LH and GOES LH in Fig. 7. In most cases, high discrepancy in total LH seems to be caused by corresponding discrepancy in the number of convective grid points, which is inevitable, but overall, total LH values seem to agree well if the

565   number of convective grid point is similar.

570
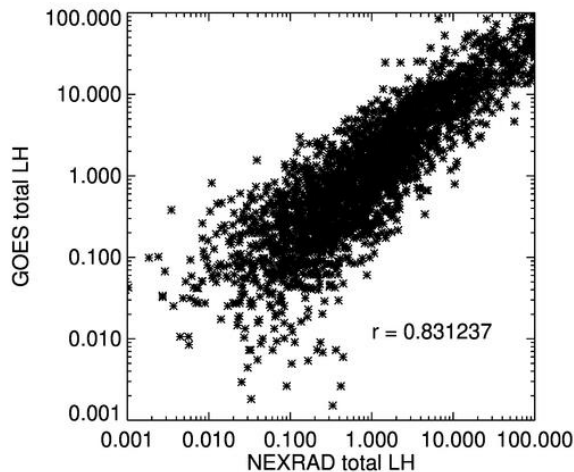
Figure 7: Scatter plot of NEXRAD total LH and GOES total LH in K/s. It is plotted in log-log axes.

575

5 Impacts of NEXRAD LH and GOES LH on precipitation forecast

The WRF model was run for one convective case on 10 July 2019 to compare impacts of GOES LH and NEXRAD LH on precipitation forecasts. HRRR data are used as initial and boundary conditions, and the same configuration is used as when making the LUT. GOES-16 visible data are only available for initialization from 15UTC to 22UTC, so results are compared after one hour of running freely, from 17UTC to 00UTC. In order to initiate convection as HRRR does with NEXRAD, modeled LH profiles are replaced with the observed LH profiles every time step during one hour pre-forecast period. Observed LH profiles at 45, 30, 15, 0 minute before the start of the free run are used for respective 15-minute period of 60-45, 45-30, 30-15, and 15-0 minute before the start of the free run. After the pre-forecast run, the model is run freely for an hour, and after the one-hour free run, the one-hour accumulated rainfall rate results are compared. One-hour rain accumulation from simulations without using any observed LH (CTL), using NEXRAD LH (NL), and using GOES LH (GL) are validated against gauge bias corrected quantitative precipitation estimation (QPE; one-hour accumulation) from MRMS.

Figure 8 shows one simulation where observed LH is applied from 15UTC to 16UTC, after which the model is freely run for an hour until 17UTC. The CTL run (Fig. 8a) misses many convective regions, and precipitation is markedly less than MRMS observations in Fig. 8b. Both the NL and GL runs initiated convection in the right place, and enhance precipitation. In the light green box region where CTL run totally misses convection, NL and GL runs both produce precipitation, although there is an overestimation in NL run while there is an underestimation of precipitation in the GL run. In the dark green box region where convection is weak in the CTL run, both NL and GL runs increased precipitation closer to the observation. The NL run correctly initiates convection in the yellow box region, but not in the red box region, while the GL run correctly initiates convection in the red box but not in the yellow box.
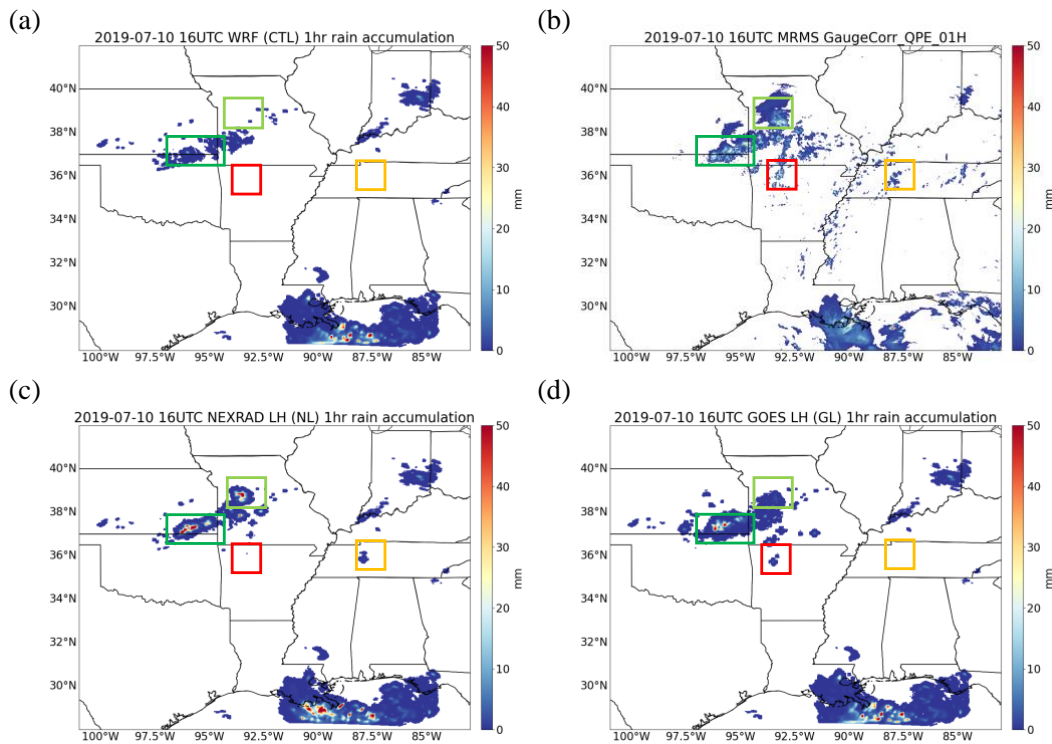
Figure 8: One-hour rain accumulation at 17UTC in 10 July 2019 from (a) a simulation without any LH observation, (b) MRMS gauge corrected quantitative precipitation estimation (QPE), (c) a simulation using NEXRAD LH, and (d) a simulation using GOES LH.

600

These results can be further explained by looking at Fig. 9, which presents maps of vertically integrated NEXRAD LH and

GOES LH that are applied to the model at 16UTC which is the last time that observed LH profiles are applied during the

15UTC-16UTC period. As seen in the enlarged two green box regions in Fig. 9, NEXRAD shows very high total LH (up to

0.35K/s) in a few grid points, and small LH in surrounding area, while most of the GOES LH values in the two green boxes are

605   at or below 0.2K/s. The reason why there was an overestimation of precipitation in the NL run (Fig. 8c) could be due to this

extremely high NEXRAD LH. Interestingly in the red box region, both NEXRAD and GOES have similar total LH values, but

only the GL run produced precipitation (in Fig. 8d). Lastly, it makes sense that GL run did not initiate convection in the yellow

box region (Fig. 8d) because no LH is applied due to missed convection by the GOES convection detection algorithm (Fig. 9b).

Overall, both NEXRAD LH and GOES LH have positive impacts on the precipitation forecast, and their forecast results appear

610   to have similar skills.

(a)   (b)

615

620
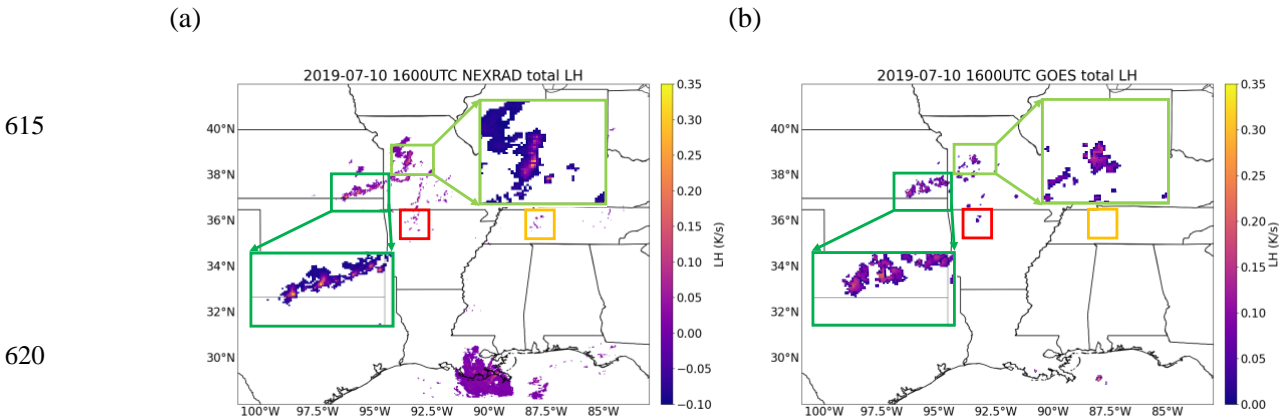
Figure 9: Vertically integrated LH at 16UTC in July 10th, 2019 from (a) NEXRAD and (b) GOES-16. Two

625   green box regions are enlarged for better comparison.

For a quantitative evaluation, Fraction Skill Scores (FSS) are calculated for the eight simulations that added LH for different one-

hour time periods (LH is added for an hour during 15-16UTC, 16-17UTC, …, 22-23UTC, and FSS are calculated after the one-

630   hour free run at 17UTC, 18UTC, …, 00UTC). FSS is one of the neighborhood-based precipitation verification metrics

introduced by Roberts and Lean, 2008, and it is calculated using Eq. (3).

$$FSS_{(n)} = 1 - \frac{\frac{1}{N_x N_y}\sum_{i=1}^{N_x}\sum_{j=1}^{N_y}[O_{i,j}-P_{i,j}]^2}{\frac{1}{N_x N_y}\left[\sum_{i=1}^{N_x}\sum_{j=1}^{N_y}O_{i,j}^2+\sum_{i=1}^{N_x}\sum_{j=1}^{N_y}P_{i,j}^2\right]},$$
                                                          (3)

where N_x and N_y are the number of columns and rows, and $O_{i,j}$ and $P_{i,j}$ are respectively an observed and model forecast fraction

calculated over a small $n \times n$ domain. It calculates a fraction that passed a threshold value over $n \times n$ domain, and the fraction

635   over the small domain is compared rather than individual grid points. In this study, a 15 km × 15 km domain is used to calculate

FSS for the six one-hour accumulated precipitation thresholds of 0.254, 2.54, 6.35, 12.7, 25.4, and 50.8 mm/hour (0.01, 0.1, 0.25,

0.5, 1, and 2 inch/hour).

640

645

650
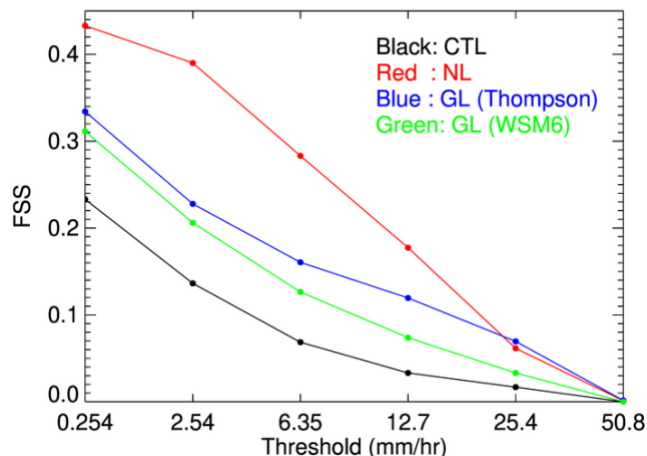
Figure 10: Fraction Skill Score (FSS) using thresholds of 0.254, 2.54, 6.35, 12.7, 25.4, and 50.8 mm/hour (0.01, 0.1, 0.25, 0.5, 1, and 2 inch/hour) for CTL (black), NL (red), GL with Thompson scheme (blue), and GL with WSM6 scheme (green) runs.

655 The overall FSS for the four simulations is shown in Fig. 10. Black, red, blue, and green lines represent CTL, NL, GL with Thompson scheme, and GL with WSM6 scheme, respectively. Compared to CTL, both NL and GL runs show significant improvements in FSS for all thresholds. Although NL run outperforms GL at smaller thresholds, GL run shows better results at higher thresholds of 25.4 and 50.8 mm/hour. This can be because GOES LH tends to have maximum heating in the middle atmosphere, which can develop deeper clouds, but further investigation is needed to study sensitivity of different vertical profiles

660 to precipitation forecast. Additional GL run using different microphysical scheme of WSM6 is provided to briefly show impacts of using different microphysical scheme. It has less positive impacts, indicating that keeping consistency in microphysical scheme could be critical. Nonetheless, it shows that LH from GOES-16 presented in this study can be useful for improving precipitation forecast especially in the regions where ground-based radar data are not available.

665 **6 Conclusions**

A method to obtain vertical profiles of LH from GOES-16 ABI data was described. Convective clouds are first detected using temporal changes in reflectance and T_b, and LH profiles for the detected cloud are found by searching a LUT created using WRF model simulations. The LUT contains LH profiles of convective clouds that are defined by a threshold of 1.5m/s for the modeled vertical velocity, and these convective LH profiles are sorted according to T_b at 11.2μm, which is a good indicator of cloud top

670 height. Mean profiles that represent each T_b bin show good correlation with cloud top temperature, with lower T_b bin having deeper LH profiles. Precipitation rates corresponding to each bin are also well correlated to T_b. Even though the LUT in Fig. 2 uses one infrared channel to estimate LH profiles, it is actually more than just one brightness value. The GOES-16 convection detection algorithm uses 10 time steps of channel 2 reflectance and channel 8 and 10 brightness temperature data to find active convective regions with bubbling cloud top and brightness temperature decrease, and thus the overall algorithm uses more

675 information than just one brightness temperature value. In addition, LH values in the LUT are well within the range that is

allowed in HRRR to initiate convection using NEXRAD, which makes it reasonable to use them to initiate convection in the forecast model.

680 To investigate how LH from GOES-16 differs from other radar products, LH from GOES-16, NEXRAD, and CSH are compared in three convective clouds with different cloud top heights. Vertical profiles of convective LH from GOES-16 are very similar to those from CSH that use model simulations in the LUT. Their vertical profiles show heating throughout the vertical layer except near the surface where evaporation occurs, and heating peaks around the middle of the atmosphere. This vertical pattern differs from when using the empirical formulation used with radar reflectivity by HRRR. Vertical profiles of LH from NEXRAD highly depend on vertical profiles of reflectivity which typically peaks near the surface in convective regions, and thus, maximum LH is

685 usually observed at lower level, which is not commonly shown in the modeled heating rate.

Even though vertical profiles of LH from the different methods differ, the total LH which is calculated by integrating the horizontal and vertical LH for each convective cloud is shown to be similar between GOES-16 and NEXRAD. The three-month analysis shows a good correlation overall between GOES-16 and NEXRAD if the detected convection areas were similar.

690 Besides the limitation in convection detection by GOES-16, GOES LH estimates can have large errors in case of multi-layer clouds or clouds with sheared structure, as it is based on the cloud top.

In order to examine impacts of GOES LH in precipitation forecast compared to NEXRAD LH, one case study is presented. Applying LH derived from GOES-16 was able to correctly initiate convection in the scene, and the simulation result looks

695 similar to the one applying NEXRAD LH. Although GOES convection detection algorithm is not perfect and misses some convection, and GOES LH is somewhat restricted to cloud top information, these results prove that LH obtained from GOES-16 have reasonable values, and it can be used to improve precipitation forecasts over the region where ground-based radar data are not available.

700 This work is a proof of concept study to show potential of using infrared data in initializing convection, and there are much room for improvements. The LUT can be improved by adding more input variables such as cloud top cooling rate. In case of using cloud top cooling rate as inputs, additional wind products will be needed for both model and observation to remove errors coming from cloud advection. Aside from changing input variables, other microphysical schemes can be tested for the LUT to compare intensities or vertical structures of the derived LH profiles using different microphysical schemes. In addition, more

705 investigation will be needed to analyze the impacts of different vertical structure of LH in convective initiation.

710

715

Appendix A

Additional LUT using composite reflectivity along with cloud top temperature is provided here. This LUT can be used with NEXRAD composite reflectivity or other synthetic radar reflectivity simulator that uses GOES-16 data such as GREMLIN. This LUT includes vertical profiles of mean reflectivity for each cloud top temperature and composite reflectivity bin (Fig. A1) as well as vertical profiles of LH (Fig. A2). Radar reflectivity profiles retrieved using this LUT can be used directly in the model initialization step as ground-based radar reflectivity profiles are used in the HRRR model, or LH profiles in this LUT can be used with some modifications in model initialization step as in this study. Each plot shows mean profiles for each cloud top temperature bin while different color in the plot represents each composite reflectivity bin. Note that for higher cloud top temperature bin, high composite reflectivity bins (red or brown lines) are not shown because clouds with warmer cloud top do not generally show high composite reflectivity, and for lower cloud top temperature bin, low composite reflectivity bin (blue line) is not shown because deep convective clouds tend to have high composite reflectivity.
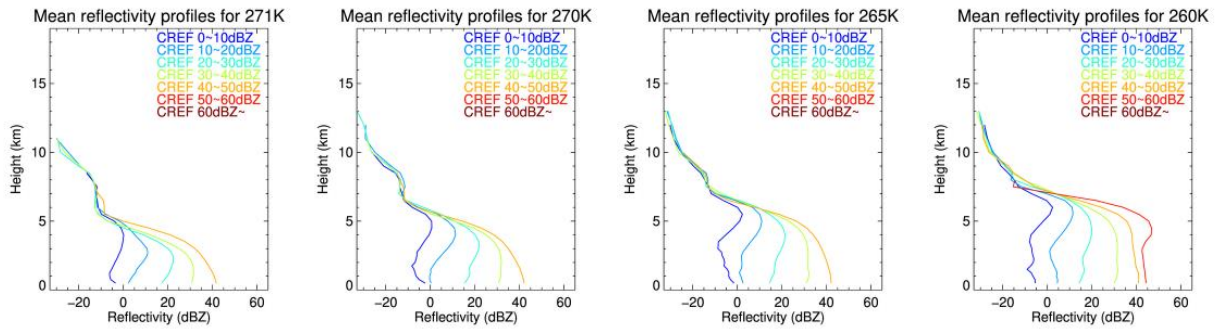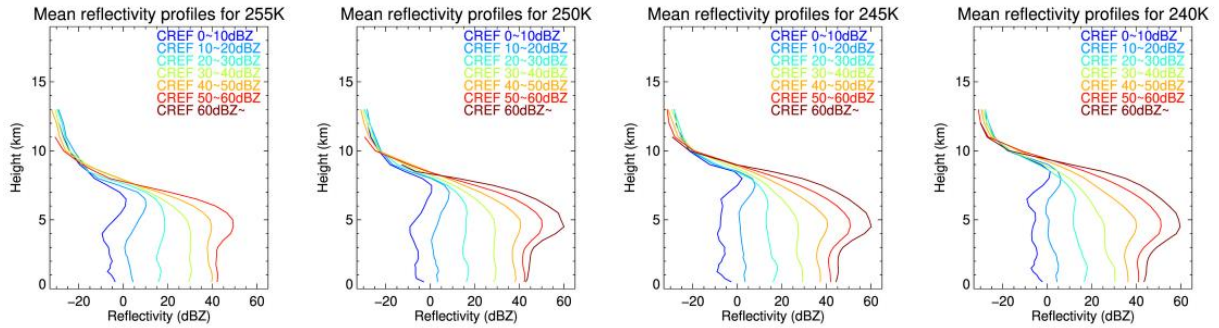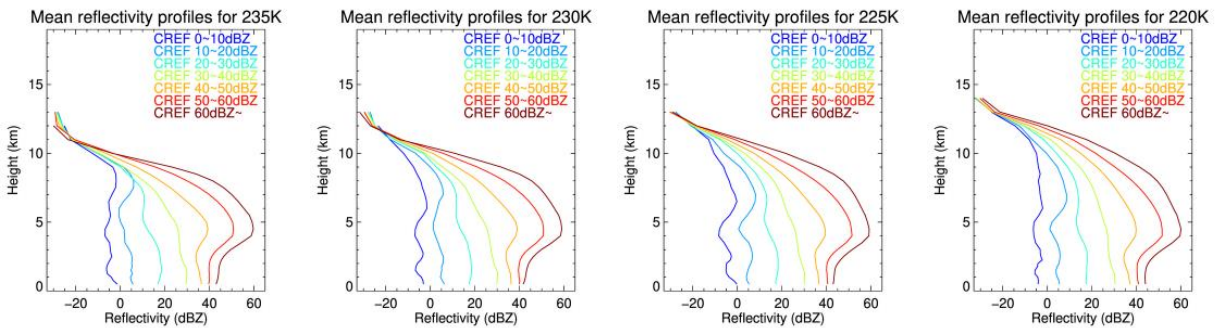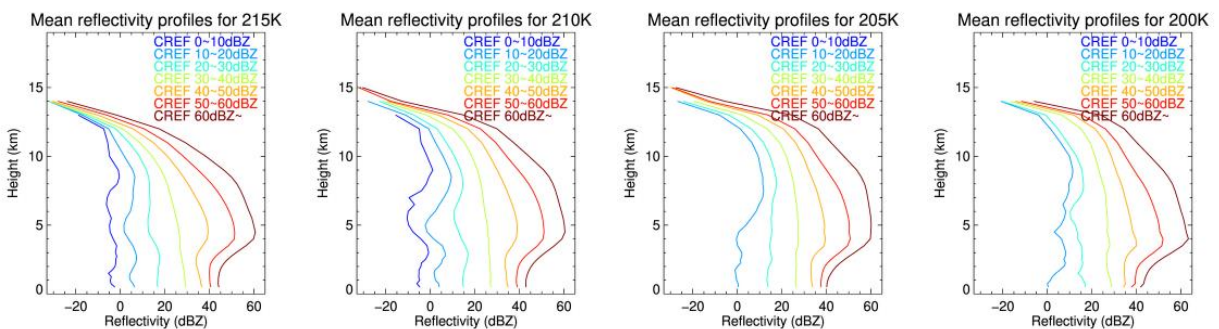
Figure A1: Mean reflectivity profiles for 16 cloud top temperature bins and 7 composite reflectivity bins. Each plot corresponds to each cloud top temperature bin, and different colors in the plot represent each composite reflectivity bin.
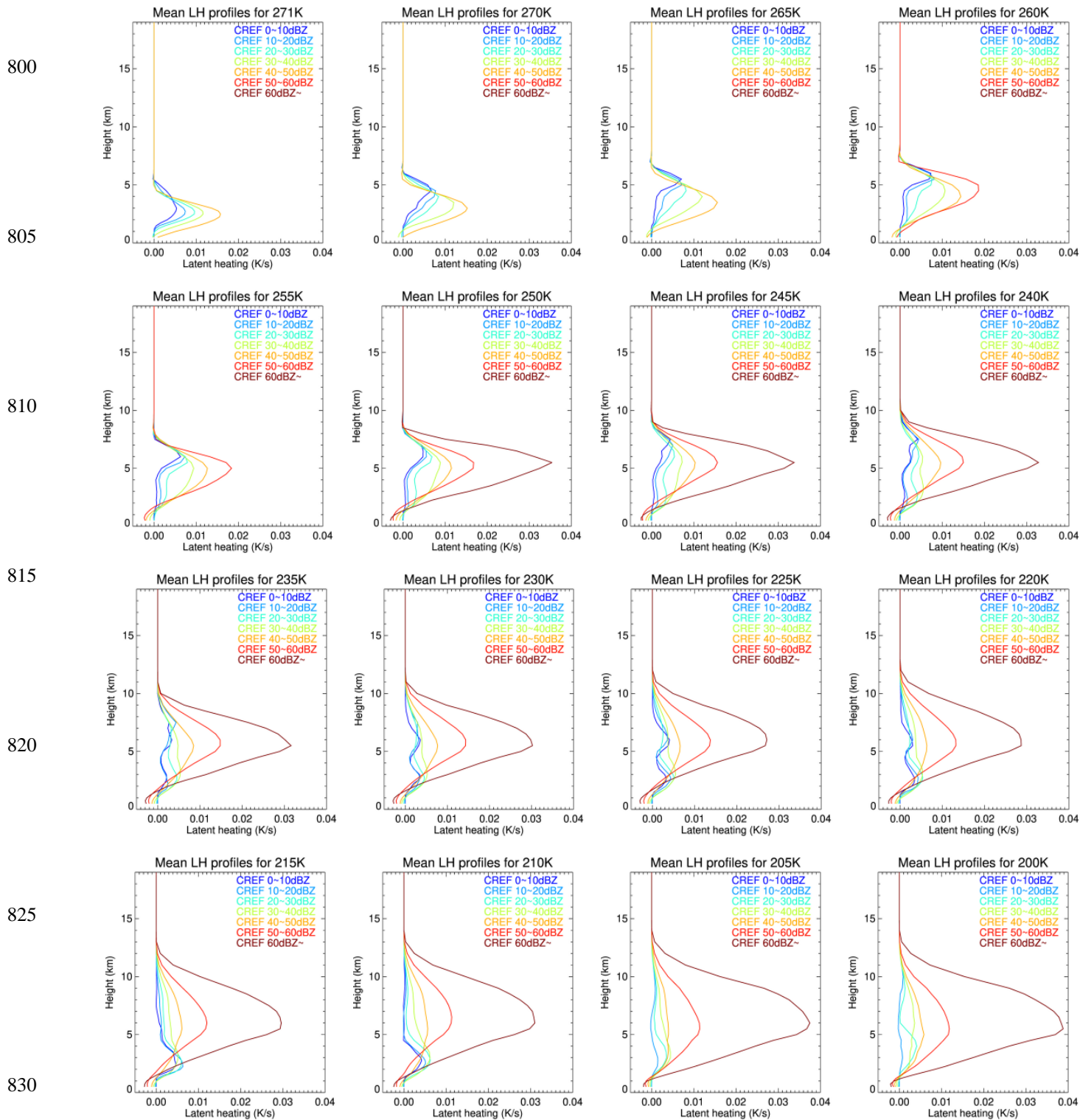
Figure A2: Mean LH profiles for 16 cloud top temperature bins and 7 composite reflectivity bins. Each plot corresponds to each cloud top temperature bin, and different colors in the plot represent each composite reflectivity bin.

Acknowledgments

This research is supported by the Cooperative Institute for Research in the Atmosphere (CIRA)'s Graduate Student Support Program.

Author contributions

All three authors contributed to the retrieval, and the manuscript was written jointly by YL, CK, and MZ.

Competing interests

The authors declare that they have no conflicts of interests.

Data availability

GOES-16 ABI brightness temperature data are obtained from CIRA, but access to the data is limited to CIRA employees. GOES-16 ABI Level 2 Cloud Top Pressure (CTP) data are obtained from NOAA National Centers for Environmental Information, Accessed: **[January 25th, 2022]**, doi:10.7289/V5D50K85. GPM DPR data are from: GPM DPR and GMI Combined Convective Stratiform Heating L3 1 month 0.5 degree x 0.5 degree V06, Greenbelt, MD, USA, Goddard Earth Sciences Data and Information Services Center (GES DISC), Accessed: **[January 25th, 2022]**, 10.5067/GPM/DPRGMI/CSH/3B-MONTH/06, GPM DPR Spectral Latent Heating Profiles L3 1 month 0.5 degree x 0.5 degree V06, Greenbelt, MD, USA, Goddard Earth Sciences Data and Information Services Center (GES DISC), Accessed: **[*January 25th, 2022*]**, 10.5067/GPM/DPR/SLH/3A-MONTH/06, and GPM DPR and GMI Combined Stratiform Heating L2 1.5 hours 5 km V06, Greenbelt, MD, USA, Goddard Earth Sciences Data and Information Services Center (GES DISC), Accessed: **[*January 25th, 2022*]**, 10.5067/GPM/DPRGMI/CSH/2H/06. Past MRMS datasets are available at https://mtarchive.geol.iastate.edu/, Accessed: **[*January 25th, 2022*]**. HRRR data is obtained from Google Cloud, https://console.cloud.google.com/marketplace/product/noaa-public/hrrr?project=python-232920&pli=1, Accessed: **[*January 25th, 2022*]**

References

Benjamin, S.G., Weygandt, S.S., Brown, J.M., Hu, M., Alexander, C.R., Smirnova, T.G., Olson, J.B., James, E.P., Dowell, D.C., Grell, G.A. and Lin, H.: A North American hourly assimilation and model forecast cycle: The Rapid Refresh. *Monthly Weather Review*, *144*(4), 1669-1694, https://doi.org/10.1175/MWR-D-15-0242.1, 2016.

875 Bytheway, J.L., Kummerow, C.D. and Alexander, C.: A features-based assessment of the evolution of warm season precipitation forecasts from the HRRR model over three years of development. *Weather and Forecasting*, *32*(5), 1841-1856, https://doi.org/10.1175/WAF-D-17-0050.1, 2017.

Chan, S.C. and Nigam, S.: Residual diagnosis of diabatic heating from ERA-40 and NCEP reanalyses: Intercomparisons with TRMM. *Journal of climate*, *22*(2), 414-428, https://doi.org/10.1175/2008JCLI2417.1, 2009.

880 Del Genio, A.D., Wu, J. and Chen, Y.: Characteristics of mesoscale organization in WRF simulations of convection during TWP-ICE. *Journal of Climate*, *25*(17), 5666-5688, https://doi.org/10.1175/JCLI-D-11-00422.1, 2012.

DeMott, C.A.: The vertical structure and modulation of TOGA COARE convection: A radar perspective, Ph.D. thesis, Colorado State University, United States, 1996.

Geer, A. J., and Coauthors: All-sky satellite data assimilation at operational weather forecasting centres. *Quart. J. Roy. Meteor.*

885 *Soc.*, **144**, 1191–1217, https://doi.org/10.1002/qj.3202, 2018.

Gustafsson, N., Janjić, T., Schraff, C., Leuenberger, D., Weissmann, M., Reich, H., Brousseau, P., Montmerle, T., Wattrelot, E., Bučánek, A. and Mile, M.: Survey of data assimilation methods for convective-scale numerical weather prediction at operational centres. *Quarterly Journal of the Royal Meteorological Society*, *144*(713), 1218-1256, https://doi.org/10.1002/qj.3179, 2018.

Hilburn, K.A., Ebert-Uphoff, I. and Miller, S.D.: Development and interpretation of a neural-network-based synthetic radar

890 reflectivity estimator using GOES-R satellite observations. *Journal of Applied Meteorology and Climatology*, *60*(1), 3-21, https://doi.org/10.1175/JAMC-D-20-0084.1, 2021.

Houze Jr, R.A.: Stratiform precipitation in regions of convection: A meteorological paradox?. *Bulletin of the American Meteorological Society*, *78*(10), 2179-2196, https://doi.org/10.1175/1520-0477(1997)078<2179:SPIROC>2.0.CO;2, 1997.

Huaman, L. and Takahashi, K.: The vertical structure of the eastern Pacific ITCZs and associated circulation using the TRMM

895 Precipitation Radar and in situ data. *Geophysical Research Letters*, *43*(15), 8230-8239, https://doi.org/10.1002/2016GL068835, 2016.

Huaman, L. and Schumacher, C.: Assessing the vertical latent heating structure of the East Pacific ITCZ using the CloudSat CPR and TRMM PR. *Journal of Climate*, *31*(7), 2563-2577, https://doi.org/10.1175/JCLI-D-17-0590.1, 2018.

Johnson, R.H.: Partitioning tropical heat and moisture budgets into cumulus and mesoscale components: Implications for

900 cumulus parameterization. *Monthly weather review*, *112*(8), 1590-1601, https://doi.org/10.1175/1520-0493(1984)112<1590:PTHAMB>2.0.CO;2, 1984.

Kummerow, C., Barnes, W., Kozu, T., Shiue, J. and Simpson, J.: The tropical rainfall measuring mission (TRMM) sensor package. *Journal of atmospheric and oceanic technology*, *15*(3), 809-817, https://doi.org/10.1175/1520-0426(1998)015<0809:TTRMMT>2.0.CO;2, 1998.

905 Lee, Y., Kummerow, C.D. and Zupanski, M.: A simplified method for the detection of convection using high resolution imagery from GOES-16. *Atmospheric Measurement Techniques Discussions*, 1-26. https://doi.org/10.5194/amt-2020-38, 2021.

LeMone, M.A. and Zipser, E.J.: Cumulonimbus vertical velocity events in GATE. Part I: Diameter, intensity and mass flux. Journal of Atmospheric Sciences, 37(11), 2444-2457, https://doi.org/10.1175/1520-0469(1980)037<2444:CVVEIG>2.0.CO;2, 1980.

910   Levizzani, V., Kidd, C., Kirschbaum, D. B., Kummerow, C. D., Nakamura, K., and Turk, F. J: *Satellite Precipitation Measurement* (Vol. 1). Springer, 897-915, 2020.

Liu, C., Shige, S., Takayabu, Y.N. and Zipser, E.: Latent heating contribution from precipitation systems with different sizes, depths, and intensities in the tropics. *Journal of Climate*, *28*(1), 186-203, https://doi.org/10.1175/JCLI-D-14-00370.1, 2015.

Luo, Z.J., Jeyaratnam, J., Iwasaki, S., Takahashi, H. and Anderson, R.: Convective vertical velocity and cloud internal vertical

915   structure: An A-Train perspective. *Geophysical Research Letters*, *41*(2), 723-729, https://doi.org/10.1002/2013GL058922, 2014.

Nelson, E.L., L'Ecuyer, T.S., Saleeby, S.M., Berg, W., Herbener, S.R. and Van Den Heever, S.C.: Toward an algorithm for estimating latent heat release in warm rain systems. *Journal of Atmospheric and Oceanic Technology*, *33*(6), 1309-1329, https://doi.org/10.1175/JTECH-D-15-0205.1, 2016.

Nelson, E.L. and L'Ecuyer, T.S.: Global character of latent heat release in oceanic warm rain systems. *Journal of Geophysical*

920   *Research: Atmospheres*, *123*(10), 4797-4817, https://doi.org/10.1002/2017JD027844, 2018.

Peckham, S.E., Smirnova, T.G., Benjamin, S.G., Brown, J.M. and Kenyon, J.S.: Implementation of a digital filter initialization in the WRF Model and its application in the Rapid Refresh. *Monthly Weather Review*, *144*(1), 99-106, https://doi.org/10.1175/MWR-D-15-0219.1, 2016.

Satoh, S., Noda, A. and Iguchi, T.: Retrieval of latent heating profiles from TRMM radar data. In *Preprints, 30th Int. Conf. on*

925   *Radar Meteorology, Munich, Germany, Amer. Meteor. Soc* (Vol. 6), https://ams.confex.com/ams/30radar/techprogram/paper_21763.htm, 21 July 2001.

Schumacher, C., Houze Jr, R.A. and Kraucunas, I.: The tropical dynamical response to latent heating estimates derived from the TRMM precipitation radar. *Journal of the Atmospheric Sciences*, *61*(12), 1341-1358, https://doi.org/10.1175/1520-0469(2004)061<1341:TTDRTL>2.0.CO;2, 2004.

930   Schumacher, C., Stevenson, S.N. and Williams, C.R.: Vertical motions of the tropical convective cloud spectrum over Darwin, Australia. *Quarterly Journal of the Royal Meteorological Society*, *141*(691), 2277-2288, https://doi.org/10.1002/qj.2520, 2015.

Seity, Y., Brousseau, P., Malardel, S., Hello, G., Bénard, P., Bouttier, F., Lac, C. and Masson, V.: The AROME-France convective-scale operational model. *Monthly Weather Review*, *139*(3), 976-991, https://doi.org/10.1175/2010MWR3425.1, 2011.

Shige, S., Takayabu, Y.N., Tao, W.K. and Johnson, D.E.: Spectral retrieval of latent heating profiles from TRMM PR data. Part

935   I: Development of a model-based algorithm. *Journal of applied meteorology*, *43*(8), 1095-1113, https://doi.org/10.1175/1520-0450(2004)043<1095:SROLHP>2.0.CO;2, 2004.

Shige, S., Takayabu, Y.N., Tao, W.K. and Shie, C.L.: Spectral retrieval of latent heating profiles from TRMM PR data. Part II: Algorithm improvement and heating estimates over tropical ocean regions. *Journal of applied Meteorology and Climatology*, *46*(7), 1098-1124, https://doi.org/10.1175/JAM2510.1, 2007.

940   Steiner, M., Houze Jr, R.A. and Yuter, S.E.: Climatological characterization of three-dimensional storm structure from operational radar and rain gauge data. *Journal of applied meteorology and climatology*, *34*(9), pp.1978-2007, https://doi.org/10.1175/1520-0450(1995)034<1978:CCOTDS>2.0.CO;2, 1995.

Tao, W.K., Lang, S., Simpson, J. and Adler, R.: Retrieval Algorithms for Estimating the Vertical Profiles of Latent Heat Release Their Applications for TRMM. *Journal of the Meteorological Society of Japan. Ser. II*, *71*(6), 685-700,

945   https://doi.org/10.2151/jmsj1965.71.6_685, 1993.

Tao, W.K., Smith, E.A., Adler, R.F., Haddad, Z.S., Hou, A.Y., Iguchi, T., Kakar, R., Krishnamurti, T.N., Kummerow, C.D., Lang, S. and Meneghini, R.: Retrieval of latent heating from TRMM measurements. *Bulletin of the American Meteorological Society*, *87*(11), 1555-1572, https://doi.org/10.1175/BAMS-87-11-1555, 2006.

Tao, W.K., Takayabu, Y.N., Lang, S., Shige, S., Olson, W., Hou, A., Skofronick-Jackson, G., Jiang, X., Zhang, C., Lau, W. and Krishnamurti, T.: TRMM latent heating retrieval: Applications and comparisons with field campaigns and large-scale analyses. *Meteorological Monographs*, *56*, 2.1-2.34, https://doi.org/10.1175/AMSMONOGRAPHS-D-15-0013.1, 2016.

Tao, W.K., Iguchi, T. and Lang, S.: Expanding the Goddard CSH algorithm for GPM: New extratropical retrievals. *Journal of applied meteorology and climatology*, *58*(5), 921-946, https://doi.org/10.1175/JAMC-D-18-0215.1, 2019.

Weygandt, S. S. and Benjamin: Radar reflectivity-based initialization of precipitation systems using a diabatic digital filter within the Rapid Update Cycle, 22nd Conf. on Weather Analysis and Forecasting/18th Conf. on Numerical Weather Prediction, Park City, Amer. Meteor Soc., 1B.7. 26 June 2007.

Wu, J., Del Genio, A.D., Yao, M.S. and Wolf, A.B.: WRF and GISS SCM simulations of convective updraft properties during TWP-ICE. *Journal of Geophysical Research: Atmospheres*, *114*(D4), https://doi.org/10.1029/2008JD010851, 2009.

Xu, K.M. and Randall, D.A.: Updraft and downdraft statistics of simulated tropical and midlatitude cumulus convection. *Journal of the Atmospheric sciences*, *58*(13), 1630-1649, https://doi.org/10.1175/1520-0469(2001)058<1630:UADSOS>2.0.CO;2, 2001.

Yanai, M., Esbensen, S. and Chu, J.H.: Determination of bulk properties of tropical cloud clusters from large-scale heat and moisture budgets. *Journal of Atmospheric Sciences*, *30*(4), 611-627, https://doi.org/10.1175/1520-0469(1973)030<0611:DOBPOT>2.0.CO;2, 1973.

Yang, S. and Smith, E.A.: Moisture budget analysis of TOGA COARE area using SSM/I-retrieved latent heating and large-scale Q 2 estimates. *Journal of Atmospheric and Oceanic Technology*, *16*(6), 633-655, https://doi.org/10.1175/1520-0426(1999)016<0633:MBAOTC>2.0.CO;2, 1999.

Zhang, C., Ling, J., Hagos, S., Tao, W.K., Lang, S., Takayabu, Y.N., Shige, S., Katsumata, M., Olson, W.S. and L'Ecuyer, T.: MJO signals in latent heating: Results from TRMM retrievals. *Journal of the atmospheric sciences*, *67*(11), 3488-3508, https://doi.org/10.1175/2010JAS3398.1, 2010.

Zipser, E.J. and Lutz, K.R.: The vertical profile of radar reflectivity of convective cells: A strong indicator of storm intensity and lightning probability?. *Monthly Weather Review*, *122*(8), 1751-1759, https://doi.org/10.1175/1520-0493(1994)122<1751:TVPORR>2.0.CO;2, 1994.